Nanoscale

ROYAL SOCIETY OF CHEMISTRY

PAPER

View Article Online
View Journal | View Issue

Cite this: *Nanoscale*, 2021, **13**, 14777

Understanding the modulation effect and surface chemistry in a heteroatom incorporated graphene-like matrix toward high-rate lithium–sulfur batteries†

Zhenxin Zhao,‡[a] Zonglin Yi,‡[b,c] Huijun Li,[a] Rajesh Pathak,[d] Xiaoqin Cheng,[a] Junliang Zhou,[a] Xiaomin Wang *[a] and Qiquan Qiao[e]

The underlying interface effects of sulfur hosts/polysulfides at the molecular level are of great significance to achieve advanced lithium–sulfur batteries. Herein, we systematically study the polysulfide-binding ability and the decomposition energy barrier of Li_2S enabled by different kinds of nitrogen (pyridinic N, pyrrolic N and graphitic N) and phosphorus (P–O, P═O and graphitic P) doping and decipher their inherent modulation effect. The doping process helps in forming a graphene-like structure and increases the micropores/mesopores, which can expose more active sites to come into contact with polysulfides. First-principles calculations reveal that the P═O possesses the highest binding energies with polysulfides due to the weakening of the chemical bonds. Besides, P═O as a promoter is beneficial for the free diffusion of lithium ions, and the pyridinic N and pyrrolic N can greatly reduce the kinetic barrier and catalyze the polysulfide conversion. The synergetic effects of nitrogen and phosphorus as bifunctional active centers help in achieving an *in situ* adsorption–diffusion–conversion process of polysulfides. Benefiting from these features, the graphene-like network achieves superior rate capability (a high reversible capacity of 954 mA h g^{-1} at 2C) and long-term stability (an ultralow degradation rate of 0.009% around 800 cycles at 5C). Even at a high sulfur loading of 5.6 mg cm^{-2}, the cell can deliver an areal capacity of 4.6 mA h cm^{-2} at 0.2C.

Received 27th May 2021,
Accepted 9th August 2021

DOI: 10.1039/d1nr03390e

rsc.li/nanoscale

Introduction

The limited energy density of the conventional lithium-ion batteries (LIBs) cannot fulfill the practical energy demands required to efficiently utilize lithium metal as an anode in next-generation LIBs.[1,2] Lithium–sulfur batteries (LSBs) have attracted great attention as one of the most promising rechargeable energy storage systems owing to their high energy density (2600 W h kg^{-1}, four times higher than LIBs), low cost (<$150 ton^{-1}), and environmentally friendly nature.[3–5] Despite these attractive features, the practical applications of LSBs are still hindered by severe problems, including the low conductivity of sulfur (5×10^{-30} S cm^{-1}), large volume expansion (76%), and the "shuttle effect" of lithium polysulfides (LiPS).[6–8] Among these issues, the shuttle effect is notoriously caused by the migration of dissolved LiPS between the cathode and anode. During shuttling, the consumption of active sulfur leads to quick capacity fading and a poor lifespan.[9] Moreover, the continuous shuttling of LiPS and the formation of an insulating layer on the cathode and anode deteriorate the performance of the electrodes.[10,11] Therefore, regulating sulfur species to reduce the shuttle effect is of great importance in developing commercial lithium–sulfur batteries.

Stabilizing and confining LiPS within the cathode has strongly emerged as one of the effective approaches.[12] Many functional materials, such as transition metal compounds, hydroxides, MXenes and conductive polymers, *etc.*,[13–15] have been introduced into the sulfur cathode to accommodate shuttling through exerting chemical interactions and/or catalytic effects. However, the use of these polar materials will increase the overall weight of the electrode (sometimes >40 wt%), reducing the gravimetric capacity of LSBs.[16,17] Besides, these materials will disrupt the electron-transporting system, leading to poor electrical conductivity. Thus, it is necessary to design materials that can simultaneously achieve superior

[a]*College of Materials Science and Engineering, Shanxi Key Laboratory of New Energy Materials and Devices, Taiyuan University of Technology, Taiyuan, 030024, PR China. E-mail: wangxiaomin@tyut.edu.cn*
[b]*CAS Key Laboratory of Carbon Materials, Institute of Coal Chemistry, Chinese Academy of Sciences, Taiyuan, 030001, PR China*
[c]*University of Chinese Academy of Sciences, Beijing, 100049, PR China*
[d]*Applied Materials Division, Argonne National Laboratory, Lemont, IL, 60439, USA*
[e]*Mechanical & Aerospace Engineering, Syracuse University, Syracuse, NY 13244, USA*
†Electronic supplementary information (ESI) available. See DOI: 10.1039/d1nr03390e
‡These authors contributed equally to this work.

adsorption/catalysis to polysulfides and favourable electrical conductivity.

Heteroatom-incorporated carbon has been applied for many diverse applications (*e.g.*, electrocatalysis, lithium/sodium-ion batteries and gas adsorption) due to its superior conductivity, light weight, high stability and low contamination.[18–20] The integrated heteroatoms (N, P) can partially enter the carbon lattice and replace the carbon atoms, improving the surface defect level, adjusting the electronic properties, and exposing numerous electrocatalytically active sites.[21] Nevertheless, many nanocarbon materials are single-end binding sites with a low level of doping. For example, although P atoms with a large atomic radius probably bring out distinct catalytic activities, they are hard to dope into the carbon networks, resulting in a low content of P doping.[22] Owing to the adsorption saturation, the low doping content of heteroatoms cannot retard the shuttle effect effectively. Phytic acid is considered as a natural and renewable biological compound and contains abundant phosphate groups; it as a P source is easily ester-crosslinked with biomass materials and achieves high P doping. Besides, the pore size effect can also greatly affect the transportation of lithium ions and the ability of LiPS blocking. Thus, rational design, high contents of atom doping and a novel micro/mesoporous structure are necessary to achieve extraordinary electrochemical performance.[23] Furthermore, deciphering the inherent modulation effect of heteroatoms and chemical interactions plays a pivotal role in understanding the interface mechanism with LiPS.

In this contribution, a N, P co-doped carbon network is successfully prepared by a simple low-temperature method with the oxyamination and esterification reaction, followed by the carbonization process to achieve remarkable electrical conductivity and strong polysulfide chemisorptivity. Dicyandiamide as a self-sacrifice template helps in forming graphene-based nanosheets. Phytic acid as a crosslinker and an activation agent is beneficial for the high doping content of P atoms and the doping process increases the specific surface area and the content of micropores. The adsorption and catalysis of heteroatoms are systematically studied by experiments and first-principles calculations. The inherent modulation effect of heteroatoms is probed to decipher the conversion kinetics of polysulfides and activation energies. Besides, Raman technology is used to further confirm the transformation process and the confinement effect of sulfur chemistry. As a result, the N, P co-doped carbon with high content doping shows a reduced activation energy of 0.24 eV and excellent electrochemical performance. The N, P co-doped carbon network delivered a high reversible capacity of 954 mA h g^{-1} at 2C and superior long-term stability with an ultralow degradation rate of 0.009% per cycle at 5C.

Experimental section

Synthesis of NPC

All reagents used were of analytical grade. Firstly, 0.5 g of glucose and 10 g of dicyandiamide (DCD) were dissolved in 250 mL of deionized water. Then 0.8 mL of phytic acid (PA) was added to the solution and stirred at 90 °C until the deionized water was removed completely. Finally, the sample was annealed at 900 °C for 2 h with a heating/cooling rate of 5 °C min^{-1} under an Ar atmosphere. The obtained sample was denoted as NPC. The N-doped carbon (NC), P-doped carbon (PC), and pure carbon (GC) were prepared with the same methods without using PA and DCD, respectively.

Synthesis of the polysulfide electrolyte and the adsorption test

For the preparation of 0.1 M Li_2S_6 solution, 0.32 g of sulfur (Sigma-Aldrich) and 0.092 g of Li_2S (Macklin) were added to 20 mL of DME solution. Then it was stirred at 60 °C in an Ar-filled glove box for 24 h. The samples with an equal surface area were added to 2 mL of Li_2S_6 solution.

Materials characterization

X-ray diffraction (XRD) was performed from 10° to 90° (Rigaku, Rint-2000) with a scan rate of 10° min^{-1}. The morphology and element distribution were analysed with a scanning electron microscope (SEM, TESCAN Czech) and transmission electron microscope (TEM, JEOL 2010). The specific surface area was determined by the Brunauer–Emmett–Teller (BET, Micromeritics) method. Raman spectra were obtained using a Renishaw inVa with a 532 nm laser. The surface chemistry of the samples was tested by X-ray photoelectron spectroscopy (XPS, Thermo K alpha). The adsorption tests were conducted using a UV-vis spectrometer.

Electrochemical measurements

For the preparation of a sulfur-containing cathode, 80% heteroatom-incorporated carbon materials (mass ratio), 10% super P and 10% PVDF (polyvinylidene fluoride) binder were mixed in NMP solution and the formed slurry was cast on a carbon cloth. Li_2S_6 was used as the active material. 400 mg of S_8 and 115 mg of lithium sulfide (Li_2S) were dispersed in 5 mL of 1 M LiTFSI in DME/DOL (v/v = 1 : 1) with 0.1 M $LiNO_3$ (normal electrolyte) and heated at 50 °C for 24 h, which was used as the catholyte. To assemble CR2025 coin cells, the carbon cloth electrode (1 cm^2) was impregnated with 20 μL of catholyte (corresponding to about 2 mg of sulfur). Celgard 2400 and Li foil were used as the separator and anode, respectively. In the control cell (CC), Li_2S_6 was added dropwise on the carbon cloth without any modifications. Cycling performance, rate performance and GITT tests were performed on a Neware CT4000-8 with a voltage window of 1.7–2.8 V. Cyclic voltammetry (CV) and electrochemical impedance spectroscopy (EIS) were carried out on the AMETEK electrochemical workstation.

Computational details

Spin-polarized density functional theory (DFT) calculations are conducted using the Vienna *ab initio* Simulation Package (VASP) 5.4. The generalized gradient approximation (GGA) using the Perdew–Burke–Ernzerhof (PBE) exchange–correlation function is chosen as the exchange–correlation interaction. The frozen-core projector augmented wave (PAW) method is

applied to describe the ion–electron interactions. The effect of dispersion is included by the empirical correction scheme of Grimme (DFT-D3). $3 \times 3 \times 1$ and $9 \times 9 \times 1$ γ k grids are used for structural optimization and self-consistent field (SCF) calculations in DFT, respectively. The electron wave functions are expanded on a plane wave basis with an energy cutoff of 400 eV. The convergence criteria of the maximum force less than 0.04 eV $Å^{-1}$ and energy changes less than 1×10^{-6} eV are employed.

To describe the adsorption energy between graphene materials and LiPS, the following formula is applied:

$$E_{ad} = E_{tot} - (E_{gr} + E_{LiPS})$$

where E_{gr} is the free energy of graphene layers, E_{LiPS} is the free energy of the LiPS molecules, and E_{tot} is the free energy of a graphene layer with LiPS adsorbates. Here, a negative E_{ad} means an attractive interaction.

Results and discussion

The synthesis procedure of NPC is illustrated in Fig. 1. The precursor was prepared by a simple low-temperature method with oxyamination and esterification reactions. Specifically, glucose is a polyhydroxy aldehyde, which is the most widely distributed and one of the most pivotal monosaccharides in nature. Dicyandiamide as a nitrogen source can react with glucose *via* oxyamination to achieve abundant nitrogen for doping.[24] Phytic acid, composed of twelve acidic protons on six P-containing units on a single six-carbon molecule, has a strong chelating ability with glucose and can be used as a P source to form an ester-crosslinking substance.[25] Then graphene-like nanosheets were synthesized by the pyrolysis approach.

The as-fabricated NPC and NC exhibit continuously smooth lamellar networks with novel characteristics such as a large size and abundant pores (Fig. 2a–d and Fig. S1a–d†). The TEM image unambiguously confirms that NPC is smoother than NC and both samples are largely amorphous. Besides, PC and GC manifest similar irregular particles with a size of about 30 μm (Fig. S1e–l†). Comparing the difference in morphology, the formation mechanism of a graphene-like structure can be roughly concluded. Firstly, the g-C_3N_4 sheets are formed by the thermal decomposition–polymerization of DCD and the carbonized glucose is covered on the g-C_3N_4 sheets during this process. Then the g-C_3N_4 sheets as a self-sacrificing template are decomposed with the increase of temperature, which further improves the content of nitrogen. The graphene-like network can provide a high-speed channel of lithium ions and ensure the uniform distribution of sulfur.

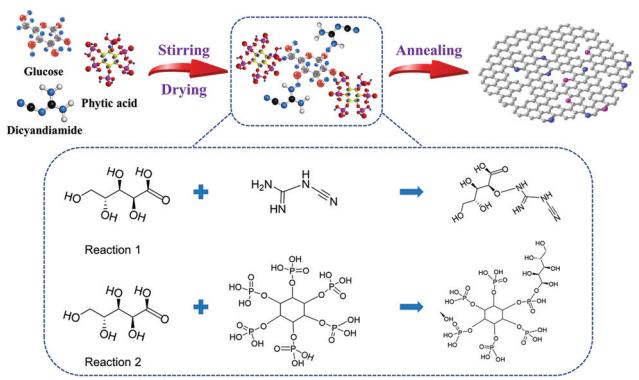

Fig. 1 Schematic illustration of the synthesis of NPC.

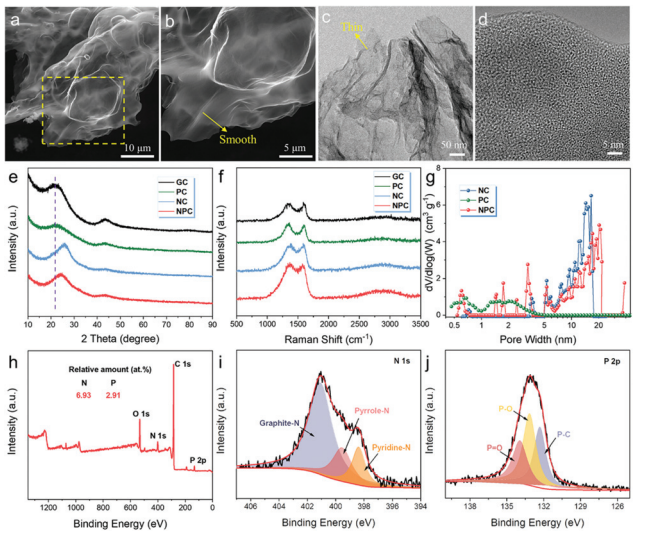

Fig. 2 Morphology and characterization of samples. SEM and TEM images of (a–d) NPC, (e) XRD patterns, (f) Raman spectra, (g) pore size distribution, (h) XPS survey spectrum of NPC and high-resolution of (i) N 1s and (j) P 2p XPS spectra.

Fig. 2e displays the XRD patterns of all samples. Two broad peaks at about 21–26° and 43.2° correspond to the diffraction of the (002) and (100) planes of carbon sheets, further demonstrating the disordered structure. According to the Bragg equation, the average (002) interlayer spaces of C, NC, PC, and NPC are 0.403, 0.394, 0.344 and 0.367 nm, respectively, which indicates that the doping of nitrogen and phosphorus heteroatoms can reduce the layer spacing. The D peak and G peak can be observed from the Raman spectra (Fig. 2f and Table S1†); the D peak is related to the disordered structure and the G peak represents the stretching vibration on the surface of the sp^2 carbon atoms.[26] The highest I_D/I_G value of NPC (1.56) compared to those of NC (1.28), PC (1.24) and GC (1.17) implies that NPC has the most abundant defects, which predict their superior adsorption ability.

The pore structures are analyzed using nitrogen adsorption–desorption isotherms (Fig. S2†). NPC and NC exhibit the typical type IV isotherms with slight hysteresis and PC shows the type I isotherm, ascribed to the micropore and mesopore adsorption. The quantified values obtained from the BET measurement are summarized in Table S2.† The specific surface areas of NC, PC and NPC are 407, 1258 and 777 $m^2\ g^{-1}$ with a total pore volume of 1.46, 0.65 and 1.52 $cm^3\ g^{-1}$, respectively. Such a large specific surface area affords a

sufficient interface as well as abundant active sites for the redox of LiPS. The pore size distribution is calculated using the DFT model (Fig. 2g). Specifically, NC is mainly composed of mesopores in the range of 5–20 nm (52%) and PC is mainly made up of micropores ranging from 0.5 to 2 nm (75%) and mesopores of 2 to 5 nm (22%). Combining the merits of NC and PC, NPC has a hierarchical porous structure (the proportion of 0.5–20 nm in 0.5–100 nm is 96%). The mesopores are formed due to the thermal decomposition of the generated g-C_3N_4 and the generated micropores can be attributed to the sublimation of P_2O_5 and red P in the activation process.[27] In detail, micropores are the ideal confined space to accommodate LiPS by physical anchoring. Mesopores are essential for increasing the sulfur loading and proving the uniform distribution of sulfur.[28,29]

To gain insight into the chemical environment and bonding states, XPS analysis is performed. The survey scans indicate that NPC contains the C, N, P and O elements (Fig. 2h), which confirms that the nitrogen and phosphorus atoms are successfully incorporated into the carbon structure. The contents of N and P are 6.93 at% and 2.91 at%, respectively, higher than those reported in many other studies.[30–32] A high doping content is beneficial for the efficient adsorption of LiPS. The consequences of the deconvolution of the high-resolution N 1s, and P 2p XPS spectra are given in Fig. 2i and j. The N 1s spectrum can be separated into three peaks, corresponding to pyridinic N (398.36 eV, 15.3%), pyrrolic N (399.53 eV, 19.5%) and graphitic N (401.07 eV, 65.2%). The P 2p spectrum can also be deconvoluted into three configurations featured with P–C (132.28 eV, 31.8%), P–O (133.12 eV, 40.6%) and P═O (133.90 eV, 27.5%).[33] The surface-enriched active sites combined with a large specific area and abundant pores make NPC a favourable sulfur host.

Fig. S3† shows the SEM images of the pure carbon cloth and the carbon cloth coated with slurries. The carbon cloth is covered by NPC on the surface, which is beneficial for the sufficient contact of NPC and polysulfides. The cooperation of nitrogen and phosphorus is anticipated to achieve an improved electrochemical performance. As shown in Fig. 3a, the efficient adsorption and redox conversion of NPC lead to a high discharge specific capacity of 1447 mA h g^{-1} at 0.1C (1C = 1672 mA h g^{-1}). When the current density is increased successively to 0.2C, 0.5C, 1C, and 2C, NPC exhibits a capacity of 1327, 1213, 1120, and 954 mA h g^{-1}, respectively. As the current density returns to 0.1C again, the specific capacity can still be recovered, indicating great reversibility.[34] In contrast, NC, PC and CC can only deliver 792, 149 and 178 mA h g^{-1}, respectively, at 2C. The charge/discharge profiles display the two obvious platforms at a different rate and the second platform can still be observed at 2C (Fig. S4†). The calculated polarization potentials in Fig. 3b show that NPC shows the smallest polarization compared to other samples, further implying the effective redox transformation induced by catalytic and adsorptive dual-heteroatom doping.[35] More importantly, such an excellent rate performance endowed by NPC outperforms many reported references (Fig. 3c).[36–47] Again, the

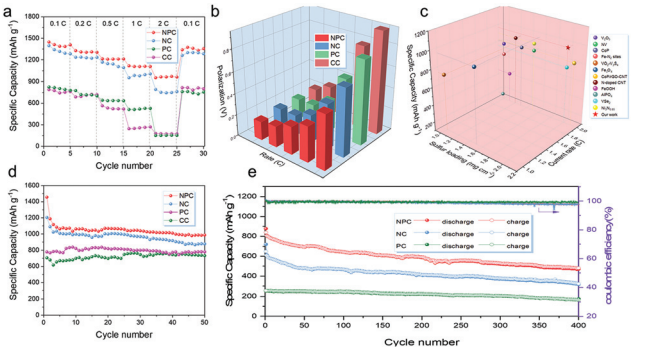

Fig. 3 Electrochemical performance. (a) Rate performance, (b) polarization potentials of different samples, (c) comparison of the rate capability with other reports; the cycling performance of (d) 0.05C and (e) 2C.

cycling performance was tested at a constant current density of 0.05C and 2C. Benefiting from the favorable immobilization of LiPS and electrocatalytic ability, NPC delivers an initial discharge capacity of 1455 mA h g^{-1} and achieves a specific capacity of 986 mA h g^{-1} after 50 cycles, much higher than NC (877 mA h g^{-1}), PC (779 mA h g^{-1}) and CC (731 mA h g^{-1}) (Fig. 3d). Besides, the cell with NPC maintains a capacity of 470 mA h g^{-1} at 2C after 400 cycles (Fig. 3e) and the long-term cycling performance at 5C elucidates an ultralow degradation rate of 0.009% per cycle (Fig. S5†), corresponding to a coulombic efficiency of more than 99%. The long-period cyclability at a high rate demonstrates the efficiency of NPC in retarding LiPS and enhancing their transformation simultaneously. Moreover, the cycling performance of NPC at high sulfur loading was also tested to validate the potential application[36] (Fig. S6†). The cell with 4 mg cm^{-2} can still hold a high reversible capacity of 949 mA h g^{-1} at 0.05C after 50 cycles and the cell with 5.6 mg cm^{-2} preserves a discharge capacity of 828 mA h g^{-1} at 0.2C after 40 cycles. The superiority in capacity is valuable for practical applications.

Identical electrodes were employed to explore the catalytic effect. As shown in Fig. S7,† the CV elucidates a larger current density, demonstrating that NPC manipulates expeditious redox kinetics of the soluble LiPS. On the other hand, NPC exhibits a lower polarization voltage than NC and PC. It suggests a reduced overpotential for LiPS transformation, confirming the electrocatalysis on the NPC catalyst.[48] Besides, the EIS plots show the lowest resistance of NPC, which is attributed to the extraordinary electrocatalytic performance.[49]

Fig. 4a and Fig. S8† present the time-resolved *in situ* Raman spectra for the discharge process. The three main peaks at about 398 cm^{-1}, 450 cm^{-1} and 509 cm^{-1} correspond to LiPS.[50,51] With the increase of the depth of discharge (DOD), the intensities of these peaks gradually become weaker and finally disappear at 100% DOD. However, the LiPS of CC show a sharp increase in the initial DOD, which is associated with the long-chain LiPS transformation to short-chain LiPS. After 100% DOD, still a small number of LiPS can be observed, con-

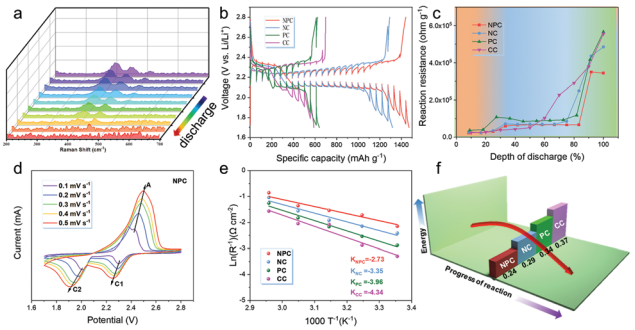

Fig. 4 Redox kinetics tests. (a) *In situ* Raman spectra of NPC, (b) GITT tests, (c) *in situ* reaction resistances during discharging, (d) CV of NPC in the scan rate range of 0.1–0.5 mV s^{-1}, (e) Arrhenius plots based on the charge-transfer resistance obtained from Nyquist plots at different temperatures, and (f) apparent activation energy calculated from (e).

firming the adequate reactions of NPC and the robust catalytic ability.[52]

Galvanostatic intermittent titration technique (GITT) curves were obtained to excavate the internal resistances during the discharging process (eqn (1)) (Fig. 4b and c).[53]

$$R = \Delta U_{\text{overpotential}}/M_{\text{mass loading}}{}^{2} \times I_{\text{current density}}. \quad (1)$$

The internal resistance increases at the initial 25% DOD, then stabilizes at about 25–80% DOD and rapidly increases at 80–100% DOD. Impressively, NPC shows favorable resistance around the whole discharge process, demonstrating the lowest interfacial reaction barriers.[54,55] The CV profiles were further obtained to compare the Li^+ diffusion of various samples (Fig. 4d and Fig. S9a–c†). The correlations between redox peak currents (I_p) and the square root of scan rates ($v^{0.5}$) are presented in Fig. S9d–f† (eqn (2)).

$$I_p = 2.69 \times 10^5 n^{1.5} A D^{0.5} C v^{0.5}. \quad (2)$$

Apparently, the fitted slopes of NPC are significantly larger than that of other samples, verifying the favorable Li^+ diffusion coefficient.[56]

To reveal the role of NPC in the energy barrier of Li^+ diffusion, temperature-dependent EIS in the range of 298–338 K (Fig. 4e, f and Fig. S10†) was carried out. According to the Arrhenius equation (eqn (3)),

$$R_{\text{int}}{}^{-1} = A \exp(-E_a/RT) \quad (3)$$

where R_{int} is the transfer resistance, A is the pre-exponential factor, E_a is the apparent activation energy and R is the universal gas constant. The derived E_a values of NPC, NC, PC and CC are 0.24 eV, 0.29 eV, 0.34 eV and 0.37 eV, respectively, implying the accelerated kinetics of Li^+ transmission.[57]

To verify the superiority of the adsorption effect, the Raman method was carried out. The heteroatom-doped carbon materials were coated on separators and a certain amount of Li_2S_6 catholyte was added dropwise on the modified separators and the electrolyte was evaporated. The Raman information was collected from the top surface to a depth of 10 μm. Fig. 5a–c show the three-dimensional reconstruction of Raman depth profiles, which provide visual discrimination of the spatial distribution for LiPS. The intensity of LiPS gradually increases from black to red. All samples (Fig. S11†) demonstrate a distinct increase in the intensity of LiPS that are concentrated at the top surface (x–y top) and the uniform distribution follows a trend of PC < NC < NPC, implying that the dual-doped carbon is beneficial for the affinity towards LiPS. Besides, the penetration depth also reveals the difference in the adsorption of LiPS. The lower penetration depth of NPC illustrates the superior ability to reduce the shuttle effect. Furthermore, the cycled Li metal was further characterized to observe the surface corrosion. The weaker LiPS intensities in Fig. S12a and b† confirm the strong physisorption and chemisorption. Nevertheless, Fig. S11c and d† show ubiquitous LiPS signals, which are rationalized by the severe shuttle effect. A visual experiment was further carried out to verify the chemical adsorption of heteroatom-incorporated carbon. As shown in Fig. 5d, the color of the Li_2S_6 solution with PC appeared to have no obvious changes. In contrast, the Li_2S_6 solution with NC and NPC almost turns transparent. The UV-vis tests show that NPC exhibits a very weak Li_2S_6 signal, unveiling the superior adsorption.

Density functional theory (DFT) calculation was conducted to understand the favorable affinity between NPC and LiPS (Li_2S_4 and Li_2S_6). The adsorption configurations for Li_2S_4 and Li_2S_6 on NPC are depicted in Fig. 5e and Fig. S13;† the strong binding sites of LiPS are inclined to bond with nitrogen and phosphorus. The calculated adsorption energies of Li_2S_4 on graphene with pyridinic N, pyrrolic N, graphitic N, graphitic P, P–O and P=O are −0.8, −1.41, −0.24, 0.03, −2.09 and −5.57 eV and the adsorption energies with Li_2S_6 are −0.77, −0.98, −0.2, 0.01, −1.62 and −5.27 eV, respectively (Fig. 5f). It is apparent that P=O functional groups show the strongest binding with LiPS, while graphitic P shows the weakest.

The electronic structures of adsorption configurations are analyzed to explain the difference in adsorption energy. The partial density of states (PDOS) of Li_2S_4 and Li_2S_6 adsorbed on

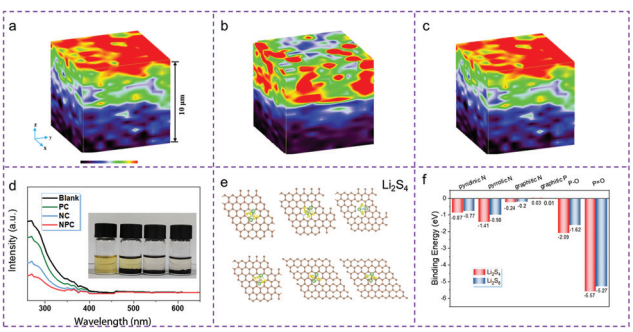

Fig. 5 Three-dimensional reconstructions of Raman depth profiles of (a) NPC, (b) NC and (c) PC; (d) UV–vis spectra; the inset shows adsorption properties in Li_2S_6 solutions, the bottles from left to right are blank, PC, NC and NPC. (e) Adsorption configurations for Li_2S_4 on NPC, and (f) calculated binding energy between different active sites and LiPS.

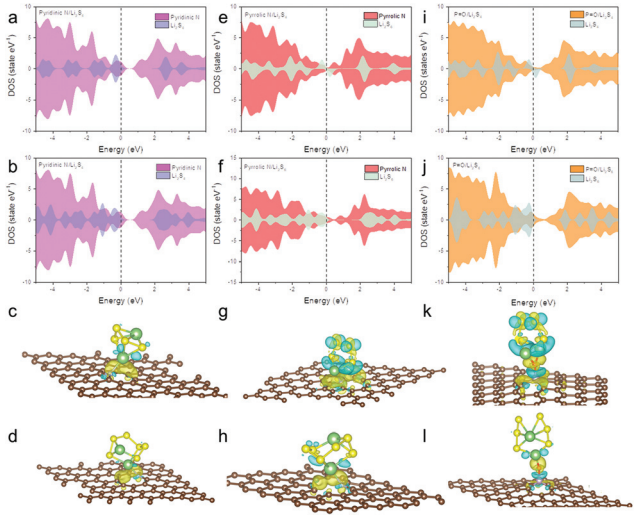

Fig. 6 Density of states patterns and electronic differential density of the theoretical model: (a–d) pyridinic N, (e–h) pyrrolic N and (i–l) P═O with Li_2S_4 or Li_2S_6. Fermi energy levels are set to zero in PDOS diagrams. Isosurfaces are set to 0.002 e per $Bohr^3$ for better observation in charge density difference figures. The yellow and blue regions represent electron gain and loss regions, respectively.

the graphene layer with pyridinic N, pyrrolic N and P═O are shown in Fig. 6 for comparison. It can be seen that the PDOS of Li_2S_4 have been polarized after adsorption with graphene containing pyrrolic N and P═O, indicating that these two functional groups have a high electronic affinity. Therefore, one of the two electrons in the highest occupied molecular orbital (HOMO) of Li_2S_4 transfers to the substrates and makes the HOMO occupied by a single electron, resulting in two peaks of α- and β-spin in the PDOS locate on both sides of the Fermi energy level, respectively. Between these two structures, P═O has more overlaps in the PDOS with Li_2S_4. In other words, the energy levels of Li_2S_4 and P═O functional groups locate more closely, suggesting a stronger binding between the adsorbed molecule and the substrate. The charge density difference figures in Fig. 6 reveal another important factor that causes the strong interaction between Li_2S_4, Li_2S_6 and P═O functional groups. The charge density difference can show the transfer orientation of electrons. For pyridinic and pyrrolic N, there are only electron gaining regions but no obvious electron loss regions between the adsorbed molecules and substrates, indicating that the formed Li–N interaction has little effect on the chemical stability of substrates. However, for P═O, except for the electron gaining regions between Li and P atoms, obvious electron loss regions appear between P and O atoms, suggesting that the Li–P interaction can lead to potential weakness of the P═O chemical bonds. Compared to pyridinic and pyrrolic N, a weakened P═O chemical bond undoubtedly enhances the Li–P interaction, making the adsorption of Li_2S_4 and Li_2S_6 stronger. The above phenomenon makes the absolute values of adsorption energy higher and thus makes P═O a good adsorption center for LiPS. For graphitic P, however, the transformation is not beneficial for LiPS adsorption. It is

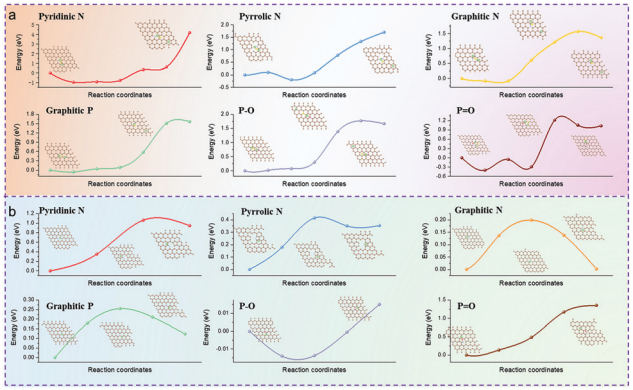

Fig. 7 Diffusion energy barriers of (a) Li_2S and (b) Li^+ on pyridinic N, pyrrolic N, graphitic N, graphitic P, P–O and P═O.

observed that the P atom moves upward and stays out of the graphene plane, but in an opposite direction, which means that the sp^2 structure of graphene is interrupted when it comes to P atoms. This might originate from the attack on dislocated π-electrons by the frontier orbital of LiPS. This leads to the weak adsorption between graphitic P and LiPS, which makes these sites deactivated for LiPS adsorption.

Furthermore, the decomposition energy barrier of Li_2S on active centers is greatly related to the reaction kinetics. As shown in Fig. 7a, the conversion process from the Li_2S molecule to the LiS cluster and a single Li^+ was calculated according to the rate-limiting step. The results indicate that the decomposition of Li_2S on pyridinic N and pyrrolic N is caused by free diffusion, and the decomposition barriers for graphitic N, P–O and P═O are 1.57, 1.77 and 1.2 eV, respectively. These results show that the N sites, especially pyridinic N and pyrrolic N, can greatly reduce the energy and kinetic barriers for polysulfide conversion, and the doped P provides a favorable reactivity for strong adsorption of polysulfides. The synergetic effects of nitrogen and phosphorus doping as bifunctional active centers help in achieving *in situ* adsorption and conversion of polysulfides. Diffusion barriers of lithium ions on graphene layers with different functional groups are also taken into consideration for better judgment. It can be seen in Fig. 7b that the lithium ion suffers diffusion barriers on graphene with graphitic N, pyridinic N, pyrrolic N and graphitic P. The energy barriers are approximately 0.2 eV to 0.4 eV for graphene with pyridinic N, graphitic N and graphitic P, and is more than 1.0 eV for graphene with pyrrolic N, indicating a very difficult lithium-ion diffusion near pyrrolic N. However, P–O and P═O show no energy barriers for lithium-ion diffusion, indicating that the presence of these two functional groups is beneficial for a free diffusion for lithium ions.

Conclusions

In this work, surface-dopant-enriched carbon networks are prepared as advanced sulfur hosts with a favorable polysulfide

affinity. For N sites, the addition of dicyandiamide as a self-sacrificing template helps in forming a graphene-like structure, which can expose more active sites to come into contact with polysulfides. The pyridinic N and pyrrolic N can efficiently accommodate the shuttle effect by forming Li–N bonding and electrocatalytically accelerate the conversion of polysulfides, and the graphitic N improves the overall electrical conductivity. For P sites, the addition of phytic acid increases the specific surface area and the content of micropores, which is beneficial for the physisorption of polysulfides. The P–O and P═O chemical bonds can form strong interactions with polysulfides. As a result, these sufficient active centers verify the conversion of sulfur chemistry and show the superior confinement effect of the polysulfides. The synergistic effects of nitrogen and phosphorus further reduce the activation energy, leading to superior rate capability (a high reversible capacity of 954 mA h g^{-1} at 2C) and long-term stability (an ultralow degradation rate of 0.009% around 800 cycles at 5C). This work sheds light on the rational design of conductive networks for high-rate electrochemical cycling performance of lithium–sulfur batteries.

Conflicts of interest

There are no conflicts to declare.

Acknowledgements

This work was supported by the National Natural Science Foundation of China (Grant No. U1710256, U1810115 and 52072256) and the Shanxi Science and Technology Major Project (Grant No. 20181102018, 20181102019, and 20201101016). The authors appreciate the support from Shiyanjia Lab (http://www.shiyanjia.com) for the XPS analysis.

References

1 R. Pathak, K. Chen, A. Gurung, K. M. Reza, B. Bahrami, J. Pokharel, A. Baniya, W. He, F. Wu, Y. Zhou, K. Xu and Q. Q. Qiao, *Nat. Commun.*, 2020, **11**, 93.
2 C. Zhao, G. L. Xu, Z. Yu, L. Zhang, I. Hwang, Y. X. Mo, Y. Ren, L. Cheng, C. J. Sun, Y. Ren, X. Zuo, J. T. Li, S. G. Sun, K. Amine and T. Zhao, *Nat. Nanotechnol.*, 2021, **6**, 166–173.
3 H. Ye, M. Li, T. Liu, Y. Li and J. Lu, *ACS Energy Lett.*, 2020, **5**, 2234–2245.
4 J. Xie, Y. W. Song, B. Q. Li, H. J. Peng, J. Q. Huang and Q. Zhang, *Angew. Chem.*, 2020, **59**, 22150–22155.
5 Z. Li, C. Zhou, J. Hua, X. Hong, C. Sun, H. W. Li, X. Xu and L. Mai, *Adv. Mater.*, 2020, **32**, 1907444.
6 Z. Ye, Y. Jiang, L. Li, F. Wu and R. Chen, *Adv. Mater.*, 2020, **32**, e2002168.
7 Z. Zhao, H. Li, R. Pathak, Z. Yang, X. Wang and Q. Qiao, *Nano Energy*, 2021, **81**, 105621.
8 D. Liu, C. Zhang, G. Zhou, W. Lv, G. Ling, L. Zhi and Q. H. Yang, *Adv. Sci.*, 2018, **5**, 1700270.
9 Y. Yang, G. Zheng, S. Misra, J. Nelson, M. F. Toney and Y. Cui, *J. Am. Chem. Soc.*, 2012, **134**, 15387–15394.
10 J. Lei, T. Liu, J. Chen, M. Zheng, Q. Zhang, B. Mao and Q. Dong, *Chem*, 2020, **6**, 2533–2557.
11 C. Zhou, Q. He, Z. Li, J. Meng, X. Hong, Y. Li, Y. Zhao, X. Xu and L. Mai, *Chem. Eng. J.*, 2020, **395**, 124979.
12 W. P. Wang, J. Zhang, J. Chou, Y. X. Yin, Y. You, S. Xin and Y. G. Guo, *Adv. Energy Mater.*, 2020, **11**, 2000791.
13 G. Chen, Y. Li, W. Zhong, F. Zheng, J. Hu, X. Ji, W. Liu, C. Yang, Z. Lin and M. Liu, *Energy Storage Mater.*, 2020, **25**, 547–554.
14 B. Li, Q. Su, L. Yu, J. Zhang, G. Du, D. Wang, D. Han, M. Zhang, S. Ding and B. Xu, *ACS Nano*, 2020, **14**, 17285–17294.
15 J. Li, Y. Xu, Y. Zhang, C. He and T. Li, *J. Mater. Chem. A*, 2020, **8**, 19544–19554.
16 H. Ye, J. Sun, S. Zhang, H. Lin, T. Zhang, Q. Yao and J. Y. Lee, *ACS Nano*, 2019, **13**, 14208–14216.
17 D. Wang, Q. Cao, B. Jing, X. Wang, T. Huang, P. Zeng, S. Jiang, Q. Zhang and J. Sun, *Chem. Eng. J.*, 2020, **399**, 125723.
18 Y. Qian, S. Jiang, Y. Li, Z. Yi, J. Zhou, T. Li, Y. Han, Y. Wang, J. Tian, N. Lin and Y. Qian, *Adv. Energy Mater.*, 2019, **9**, 1901676.
19 F. Razmjooei, K. P. Singh, D.-S. Yang, W. Cui, Y. H. Jang and J.-S. Yu, *ACS Catal.*, 2017, **7**, 2381–2391.
20 Z. Fan, B. Ding, H. Guo, M. Shi, Y. Zhang, S. Dong, T. Zhang, H. Dou and X. Zhang, *Chemistry*, 2019, **25**, 10710–10717.
21 Z. Yang, Y. Gao, Z. Zhao, Y. Wang, Y. Wu and X. Wang, *J. Power Sources*, 2020, **474**, 228500.
22 Y. Gao, Z. Yang, Y. Wang and X. Wang, *Electrochim. Acta*, 2021, **368**, 137646.
23 R. Pathak, Y. Zhou and Q. Qiao, *App. Sci.el*, 2020, **10**, 4185.
24 L. Zhang, D. Liu, Z. Muhammad, F. Wan, W. Xie, Y. Wang, L. Song, Z. Niu and J. Chen, *Adv. Mater.*, 2019, **31**, e1903955.
25 J. Bai, B. Xi, H. Mao, Y. Lin, X. Ma, J. Feng and S. Xiong, *Adv. Mater.*, 2018, **30**, e1802310.
26 Z. Zhao, H. Li, Z. Yang, S. Hao, X. Wang and Y. Wu, *J. Alloys Compd.*, 2020, **817**, 152751.
27 C. Li, Z. Chen, Y. Ni, F. Kong, A. Kong and Y. Shan, *J. Mater. Chem. A*, 2016, **4**, 14291–14297.
28 L. Huang, J. Li, B. Liu, Y. Li, S. Shen, S. Deng, C. Lu, W. Zhang, Y. Xia, G. Pan, X. Wang, Q. Xiong, X. Xia and J. Tu, *Adv. Funct. Mater.*, 2020, **30**, 1910375.
29 Y. Zheng, S. Zheng, H. Xue and H. Pang, *J. Mater. Chem. A*, 2019, **7**, 3469–3491.
30 M. Yi, B. Lu, X. Zhang, Y. Tan, Z. Zhu, Z. Pan and J. Zhang, *Appl. Catal., B*, 2021, **283**, 119635.
31 X. Hao, X. An, A. M. Patil, P. Wang, X. Ma, X. Du, X. Hao, A. Abudula and G. Guan, *ACS Appl. Mater. Interfaces*, 2021, **13**, 3738–3747.

32 X. Wang, X. Xi, G. Huo, C. Xu, P. Sui, R. Feng, X.-Z. Fu and J.-L. Luo, *J. Energy Chem.*, 2021, **53**, 49–55.
33 M.-Q. Guo, J.-Q. Huang, X.-Y. Kong, H.-J. Peng, H. Shui, F.-Y. Qian, L. Zhu, W.-C. Zhu and Q. Zhang, *New Carbon Mater.*, 2016, **31**, 352–362.
34 R. Pathak, K. Chen, A. Gurung, K. M. Reza, B. Bahrami, F. Wu, A. Chaudhary, N. Ghimire, B. Zhou, W. H. Zhang, Y. Zhou and Q. Qiao, *Adv. Energy Mater.*, 2019, **9**, 1901486.
35 Y. Li, Z. Li, C. Zhou, X. Liao, X. Liu, X. Hong, X. Xu, Y. Zhao and L. Mai, *Chem. Eng. J.*, 2021, **422**, 130107.
36 R. Liu, W. Liu, Y. Bu, W. Yang, C. Wang, C. Priest, Z. Liu, Y. Wang, J. Chen, Y. Wang, J. Cheng, X. Lin, X. Feng, G. Wu, Y. Ma and W. Huang, *ACS Nano*, 2020, **14**, 17308–17320.
37 C. Qi, Z. Li, C. Sun, C. Chen, J. Jin and Z. Wen, *ACS Appl. Mater. Interfaces*, 2020, **12**, 49626–49635.
38 Y. Qiu, L. Fan, M. Wang, X. Yin, X. Wu, X. Sun, D. Tian, B. Guan, D. Tang and N. Zhang, *ACS Nano*, 2020, **14**, 16105–16113.
39 S. D. Seo, S. Yu, S. Park and D. W. Kim, *Small*, 2020, **16**, e2004806.
40 Z. Su, M. Chen, Y. Pan, Y. Liu, H. Xu, Y. Zhang and D. Long, *J. Mater. Chem. A*, 2020, **8**, 24117–24127.
41 R. Sun, Y. Bai, M. Luo, M. Qu, Z. Wang, W. Sun and K. Sun, *ACS Nano*, 2020, **15**, 739–750.
42 Y. Dai, W. Zheng, X. Li, A. Liu, W. Zhang, X. Jiang, X. Wu, J. Tao and G. He, *ACS Appl. Mater. Interfaces*, 2021, **13**, 2521–2529.
43 B. Wei, C. Shang, X. Wang and G. Zhou, *Small*, 2020, **16**, e2002789.
44 D.-L. Vu, N. Kim, Y. Myung, M. Yang and J.-W. Lee, *J. Power Sources*, 2020, **459**, 228068.
45 W. Tian, B. Xi, Y. Gu, Q. Fu, Z. Feng, J. Feng and S. Xiong, *Nano Res.*, 2020, **13**, 2673–2682.
46 Z. Shen, Z. Zhang, M. Li, Y. Yuan, Y. Zhao, S. Zhang, C. Zhong, J. Zhu, J. Lu and H. Zhang, *ACS Nano*, 2020, **14**, 6673–6682.
47 X. Liu, Z. Li, X. Liao, X. Hong, Y. Li, C. Zhou, Y. Zhao, X. Xu and L. Mai, *J. Mater. Chem. A*, 2020, **8**, 12106–12113.
48 B.-Q. Li, H.-J. Peng, X. Chen, S.-Y. Zhang, J. Xie, C.-X. Zhao and Q. Zhang, *CCS Chem.*, 2019, **1**, 128–137.
49 Z. Zhao, R. Pathak, X. Wang, Z. Yang, H. Li and Q. Qiao, *Electrochim. Acta*, 2020, **364**, 137117.
50 H. Ci, J. Cai, H. Ma, Z. Shi, G. Cui, M. Wang, J. Jin, N. Wei, C. Lu, W. Zhao, J. Sun and Z. Liu, *ACS Nano*, 2020, **14**, 11929–11938.
51 Z. Shi, Z. Sun, J. Cai, Z. Fan, J. Jin, M. Wang and J. Sun, *Adv. Funct. Mater.*, 2020, **31**, 2006798.
52 M. Waqas, Y. Han, D. Chen, S. Ali, C. Zhen, C. Feng, B. Yuan, J. Han and W. He, *Energy Storage Mater.*, 2020, **27**, 333–341.
53 J. Zhou, X. Liu, L. Zhu, J. Zhou, Y. Guan, L. Chen, S. Niu, J. Cai, D. Sun, Y. Zhu, J. Du, G. Wang and Y. Qian, *Joule*, 2018, **2**, 2681–2693.
54 S. J. Kim, Y. Jeoun, J. Park, S. H. Yu and Y. E. Sung, *Nanoscale*, 2020, **12**, 15466–15472.
55 H. Li, X. Wang, Z. Zhao, R. Pathak, S. Hao, X. Qiu and Q. Qiao, *J. Mater. Sci. Technol.*, 2021, DOI: 10.1016/j.jmst.2021.05.034.
56 J. H. Park, W. Y. Choi, J. Yang, D. Kim, H. Gim and J. W. Lee, *Carbon*, 2021, **172**, 624–636.
57 L. Peng, Z. Wei, C. Wan, J. Li, Z. Chen, D. Zhu, D. Baumann, H. Liu, C. S. Allen, X. Xu, A. I. Kirkland, I. Shakir, Z. Almutairi, S. Tolbert, B. Dunn, Y. Huang, P. Sautet and X. Duan, *Nat. Catal.*, 2020, **3**, 762–770.

